Journal of Advanced Research 33 (2021) 99–108

Contents lists available at ScienceDirect

Journal of Advanced Research

journal homepage: www.elsevier.com/locate/jare

Understanding mechanisms of shape memory function deterioration for nitinol alloy during non-equilibrium solidification by electron beam

Guoqing Chen [a,*], Junpeng Liu [a], Zhibo Dong [a], Yulong Li [b], Yuxing Zhao [c], Binggang Zhang [a], Jian Cao [a,**]

[a] State Key Laboratory of Advanced Welding and Joining, Harbin Institute of Technology, Harbin 150001, China
[b] Beijing Institute of Space Launch Technology, Beijing 100076, China
[c] Aerospace Research Institute of Materials & Processing Technology, Beijing 100076, China

GRAPHICAL ABSTRACT

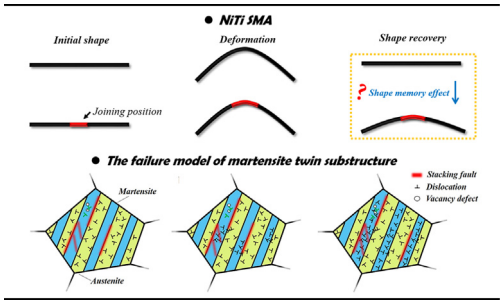

ARTICLE INFO

Article history:
Received 5 September 2020
Revised 24 January 2021
Accepted 22 February 2021
Available online 25 February 2021

Keywords:
Non-equilibrium solidification
Electron beam
Nitinol shape memory alloy
Phase transformations
Dislocations

ABSTRACT

Introduction: As an important advanced functional material, the memory effect of nitinol shape memory alloy (SMA) is the focus of research. According to the current research, the memory function of the alloy decreases after welding, and there is no sufficient explanation for the phenomenon.
Objectives: For the problem, this research is to explore the underlying causes of the decrease of shape memory function after welding by analyzing the microstructure and micro defects.
Methods: The vacuum electron beam welding tests of 1 mm thick $Ni_{50}Ti_{50}$ alloy plate was carried out to determine the appropriate welding process parameter. And the shape memory function of the welded joint was compared with that of the base metal to analyze the change of memory function.
Results: It was found that the shape memory function of the welded joint decreased significantly under different strain variables. And the phase transition temperature also changed.
Conclusions: This was due to the micro stress field produced by non-equilibrium solidification in molten pool promoted the formation and propagation of dislocations, increasing the dislocation density in the martensite. Dislocations entangled with each other in the martensite, showing a grid-like distribution, which destroyed the integrity of martensite substructure. At the same time, the twin substructure of martensite was often accompanied by vacancies, dislocations, stacking faults, and a consequently large stress field formed between twin planes due to lattice distortion. Secondary twin was identified inside martensite under micro shear stress, where the martensite showed the bending state. The habitual

Peer review under responsibility of Cairo University.
* Corresponding author.
** Corresponding author.
E-mail addresses: chenguoqing@hit.edu.cn (G. Chen), zhangbg@hit.edu.cn (B. Zhang), cao_jian@hit.edu.cn (J. Cao).

https://doi.org/10.1016/j.jare.2021.02.007

relationship between martensite phase and parent phase was destroyed, resulting in the decrease of shape memory function.

Introduction

Nitinol shape memory alloy, which has become the most widely used shape memory material, exhibits many characteristics, such as excellent wear resistance, good corrosion resistance, decent high damping and super elasticity [1–3]. The application of materials, however, is not only related to their own properties, but also to their structures [4,5]. For some special structural parts in aerospace field like air intake and exhaust control system of aircraft engine, helicopter rotor control system, and space deployable structure, welding is needed to achieve effective connection. In recent years, reliable joining for nitinol alloy has gradually become a research hotspot [6–8].

Different from the traditional materials, it is more difficult for nitinol alloy joining, since the nitinol alloy welded joints must be characterized by not only good mechanical properties, but also excellent functional characteristics [9,10]. In addition, nitinol shape memory alloy has the poor thermal conductivity and high sensitivity to impurity elements, which lead to the problems of phase transition temperature change, joint softening, brittle phase precipitation and functional deterioration [11–13]. Due to the large heat input and excessive heat affected zone present by traditional fusion welding, joint softening is distinctly discernible. Even worse, the super elasticity and shape memory effect are dramatically deteriorated. Compared to the traditional joining method, high energy beam welding possesses the characteristics of small heat input, high energy density and high processing accuracy [14–16]. The negligible heat affected zone effectively reduces the volume of the joint, showing great advantages in achieving high-quality nitinol alloy joining.

Researchers have carried out the research on high energy beam welding of nitinol shape memory alloy. It is found that joint softening still exists, corresponding to the consequently decreased microhardness, tensile strength and toughness [17–19]. This is mainly attributed to the grain growth, brittle phase precipitation, the impurity, porosity and microcrack defects inside the fusion zone [20,21]. By vacuum protection and optimized welding parameters, the strength value of the joint can reach 80% of the base metal [22,23].

High energy beam welding has different effects on the phase transition temperature of nitinol alloy, meaning the different variation trends [24,6,25]. The phase transition temperature in the fusion zone fluctuates compared to that of the base metal, which is mainly due to the change in element content in view of elements evaporation, the impurity elements, and the Ni_xTi_y ($NiTi_2$, Ni_4Ti_3, Ni_3Ti) brittle phase precipitates [26–29]. The phase transition temperature is, additionally, affected by welding thermal stress, grain size and the addition of alloying elements. Researchers pay more attention to the shape memory effect after welding considering the functionality of nitinol alloy. Even though the shape memory effect of welded joint can still maintain a relatively high level investigated by the early researches [30,31], the shape memory effect of the welded joint still depends predominately on the specific value of applied strain, as the recovery rate decreases drastically with the increased applied strain. At present, it is considered that the welding thermal stress, large plastic deformation in the fusion zone and the increase of dislocation density are the main reasons for the decrease in memory properties [6,9].

It can be seen that the current research on joining of nitinol shape memory alloy mainly focuses on the microstructure, mechanical properties, phase transition temperature and memory effect of the joint. Most of the researches are related to welding defects, microstructure, precipitated phase and element content changes. However, there is a lack of the change in martensite phase structure and interaction with micro defects, such as vacancies, dislocations and stacking faults. In this study, the evolution of martensite phase was studied, and the interaction between micro defects and martensite phase was revealed to explain the deterioration of shape memory function.

Experiments

The $Ni_{50}Ti_{50}$ shape memory alloy was welded as the base metal, which was hot rolling state with the size of 90 mm by 30 mm by 1 mm. Electron beam welding was carried out using MEDARD45 welding machine. This machine includes a vacuum system housed in a chamber with a $5x10^{-4}$ torr vacuum, and a 60 kW-55 kV electron beam gun. In order to avoid the contamination of the oxide, the base metal was polished using emery papers, and, subsequently, washed by acetone before the welding. The special fixture was used to fix the base metal plates, ensuring that the distance between two butt surfaces was less than 0.2 mm. The schematic diagram is shown in Fig. 1a. The welding parameters are shown in Table 1. The size of the test sample of shape memory function is shown in Fig. 1b.

The shape memory function of welded joints was tested using the specific test process and procedures as shown in Fig. 2. Firstly, the tensile specimens of welded joints were clamped on the tensile testing machine. The tensile strains of 4%, 6% and 8% were respectively set, which the loading speed was 1 mm/min. The specimen placement for uniaxial tensile test is shown in Fig. 2b. After the tensile test, the tested samples were put into the resistance furnace for heating, where the heating temperature was 150 ℃ and the time was 20 min, as shown in Fig. 2c. Finally, the length of each sample was tested to evaluate the shape memory function.

A VHX-1000 ultra-depth optical microscope was used to observe the microstructure of the joint. A Talos F200X in situ transmission electron microscope was used to analyze the internal substructure, precipitated phases and dislocation morphology of welded joints. An instron5569 universal testing machine was used to investigate the shape memory function of welded joints and base metal. DSC measurements were carried out at the temperature ranging from −50 °C to 150 °C with 10 K/min heating/cooling rate in a nitrogen atmosphere.

Results and discussion

Phase transition analysis

The phase transition temperatures of base metal and welded joints were analyzed, as shown in Fig. 3. Two transformation peaks, the transformation from B19′ phase to B2 phase in heating process and the reverse transformation in cooling process, were observed to be present, meaning the absence of R phase transformation between the base metal and the welded joint during the heating and cooling process (Fig. 3a). An obvious phase transformation hysteresis, where temperature was 17.9 K, was detected in base metal. In contrast to the base metal, the hysteresis range of phase

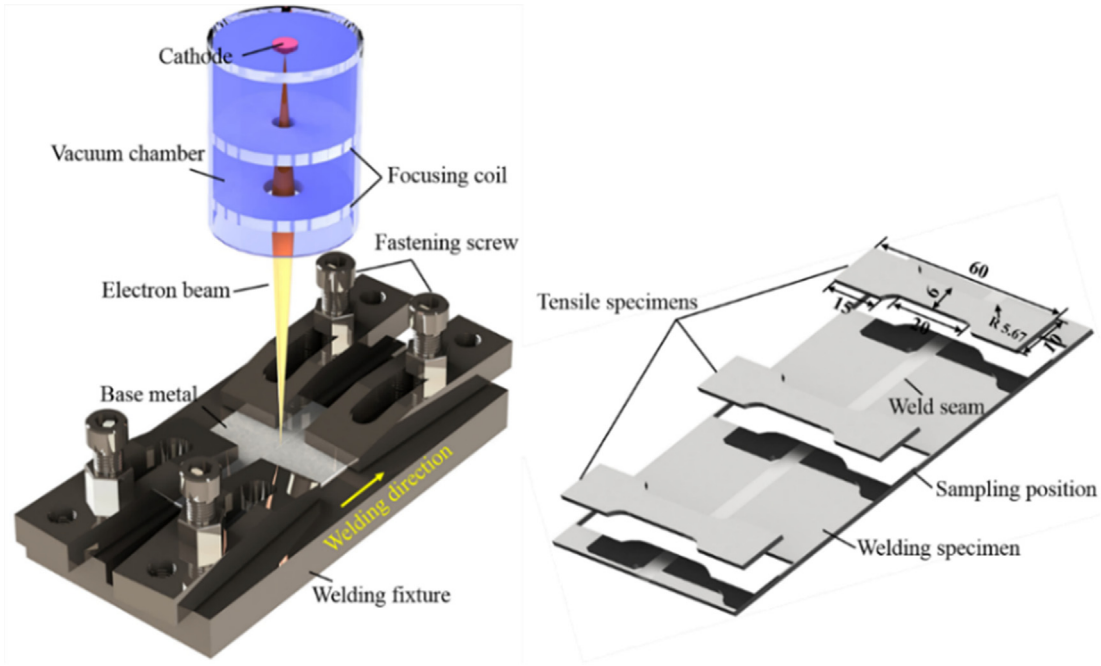

Fig. 1. Electron beam welding and test samples diagram. (a) Welding samples assembly diagram. (b) The size of test samples.

Table 1
Welding parameters.

Test number	Acceleration voltage U/(kV)	Focus current I_f/(mA)	Welding beam current I_b/(mA)	Welding speed v/(mm·min^{-1})
T1	55	2500	6–8	480
T2	55	2500	8–10	480
T3	55	2500	3–5	480
T4	55	2500	6	720
T5	55	2500	8	720

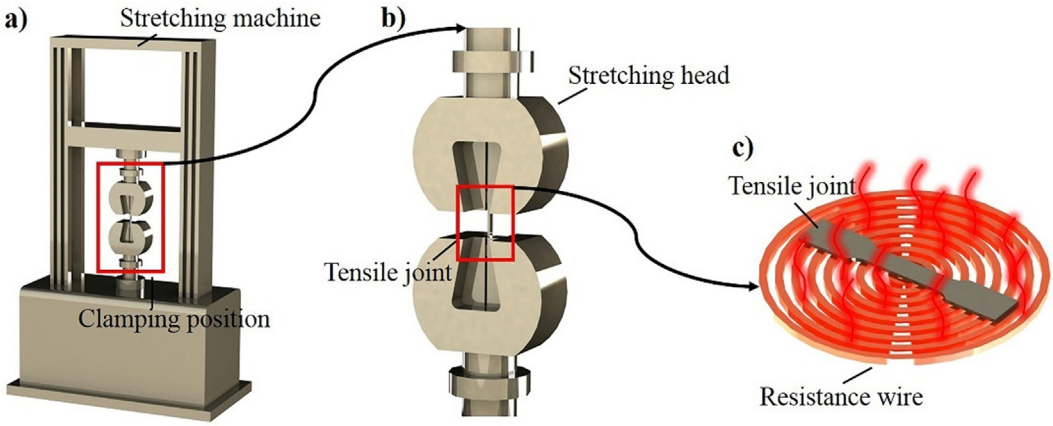

Fig. 2. The test process of shape memory function of welded joints. (a) Tensile test with constant strain. (b) Enlarged diagram of uniaxial tension. (c) Heat treatment recovery.

transformation temperature in welded joint was dramatically decreased to 3.3 K, even indicating the disappearance of interval that corresponded to beam current of 10 mA and welding speed of 480 mm/min, which is shown in Fig. 3b. The terminated temperatures (M_f and A_f) of martensite and austenite transformation, additionally, were also changed inside the welded joint. The phase transformation temperature of A_f was increased, ranging from 14.92 K to 20.62 K. Inversely, the phase transformation temperature of M_f was slightly reduced, of which the range was 3.59 to 7.05 K.

Shape memory function analysis

From the analysis of phase transition temperature, the change in welding process had little effect on the phase transition temperature of welded joints. In view of the low thermal conductivity of nitinol alloy, the process parameter T5 was selected as the appropriate process to ensure the forming of the welded joints and small heat effect. Further analysis was carried out based on T5. The shape memory function of welded joints and base metal was analyzed, as shown in Fig. 4. In this paper, uniaxial tensile tests with 4%, 6%, 8%

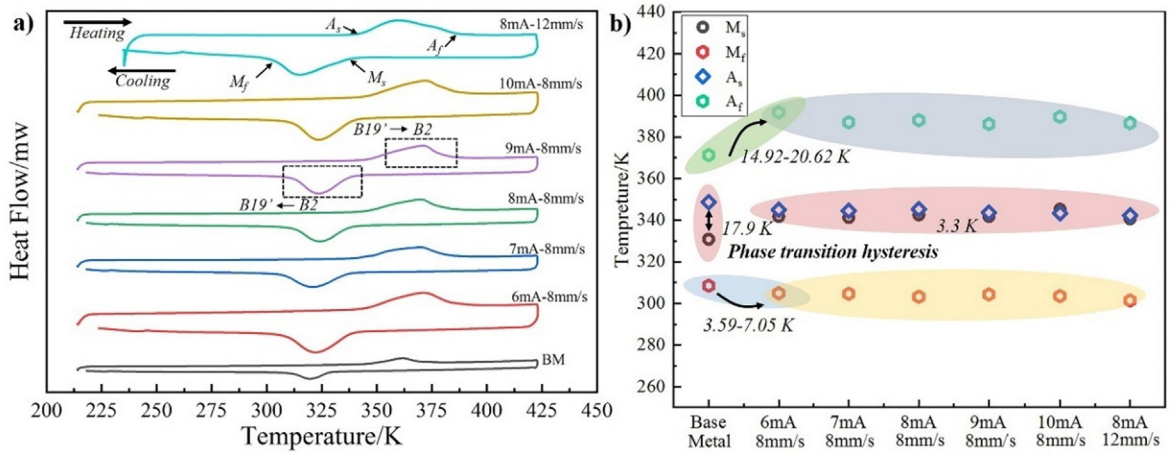

Fig. 3. DSC curves and phase transition temperature. (a) The DSC curves of base metal and welded joints. (b) phase transition temperature of base metal and welded joints.

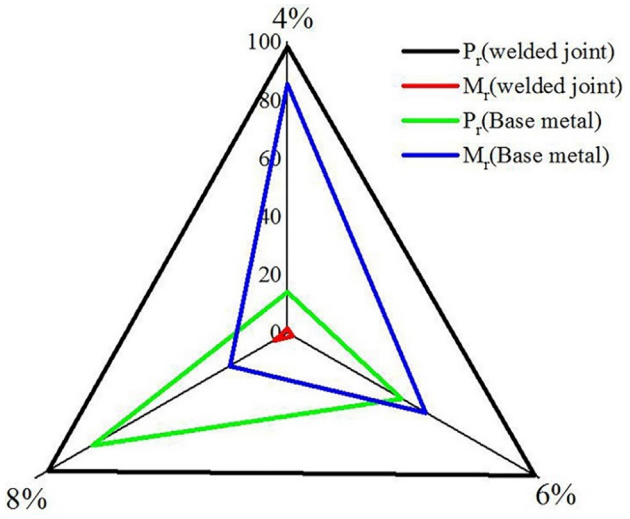

Fig. 4. The shape memory function of welded joints and base metal.

strain were carried out. P_r represented the permanent strain while M_r meant the recovery strain. It can be seen that the shape memory function of $Ni_{50}Ti_{50}$ was dramatically deteriorated after welding, compared to the base metal. At 4% strain, the shape memory recovery of base metal was 85.54%, which was in discernible contrast to 1.64% indicated by welded joints. When the strain was 6%, the shape memory recovery of base metal was decreased to 54.77%. The recovery of welded joints, meanwhile, remained stable value as 2.01%. Even though the recovery of base metal was decreased to 22.78% when the deformation was escalated to 8%, the recovery of joints was unexpectedly increased to 5.18%. Since the clamping part of the extensometer was the whole weld and a small amount of base metal, when the deformation was large, the base metal also deformed, resulting in slight increase in the recovery of welded joints. It can be seen that compared with the base metal, the shape memory function of the welded joint was substantially deteriorated. The phenomenon will be analyzed in detail in the following section.

Microstructure analysis

The microstructures in different zones are shown in Fig. 5a. The welded joint was divided into base metal zone (BMZ), heat affected zone (HAZ) and fusion zone (FZ), where the fusion zone was further divided into F1 zone that was adjacent to fusion line, F2 zone that was far from the fusion line, and the center of fusion zone, F3 zone. It can be seen that the base metal was characterized by typical convex microstructure, as shown in Fig. 5b. Compared with the base metal, the grains in heat affected zone grew up under the heat produced by electron beam, of which the breadth was 689 μm, as shown in Fig. 5c.

The microstructure of F1 zone was exhibited in Fig. 5d. Fusion line was the boundary of the fusion zone and heat affected zone, where the intense undercooling was favorable for the grains to nucleate and grow up. The morphology of the grains was mainly determined by the concentration of solute C_o, the crystallization rate R_o and the temperature gradient G of the liquid phase. As the heat dissipation capacity of one side was strong, the supercooling degree of liquid metal was high when it extended to the interior along the fusion line, which was beneficial to the growth of dendrites. The grains grew up along the normal direction of fusion line in a manner of dense columnar crystals, of which the growth range was 318 μm.

With the growth of the dense columnar crystals, the temperature gradient was gradually decreased as was expected from the heat accumulation at the solid–liquid interface, indicating that the length of the columnar crystals was shortened to change into the cellular crystals. The growth angle along the growing direction of columnar crystal was deflected by 28.5°, meaning that the cellular crystal zone occupied the majority of the fusion zone, as shown in Fig. 5e. As the bilateral cellular crystals grew to the center of fusion zone, only the upper zone was in liquid state, resulting in that the nucleated grains grew up to the top. The grains with vertical orientation are, therefore, formed in the center of the fusion zone [15], as shown in Fig. 5f, g. Scanning electron microscope was used to analyze the grain morphology of the fusion zone. From the edge to the center of the fusion zone, the grain morphology changed from the columnar crystal growing perpendicular to the fusion line to the columnar crystal with vertical orientation, as shown in Fig. 5h-j.

Precipitates and element content analysis

The microstructure and precipitated phase inside welded joint were analyzed, as shown in Fig. 6. Numerous columnar crystals were identified at the edge and center of the fusion zone. The element composition in the grains was analyzed by EDS (position P_1), indicated that the content of titanium element was slightly decreased compared with that of the base metal (P_4), as shown

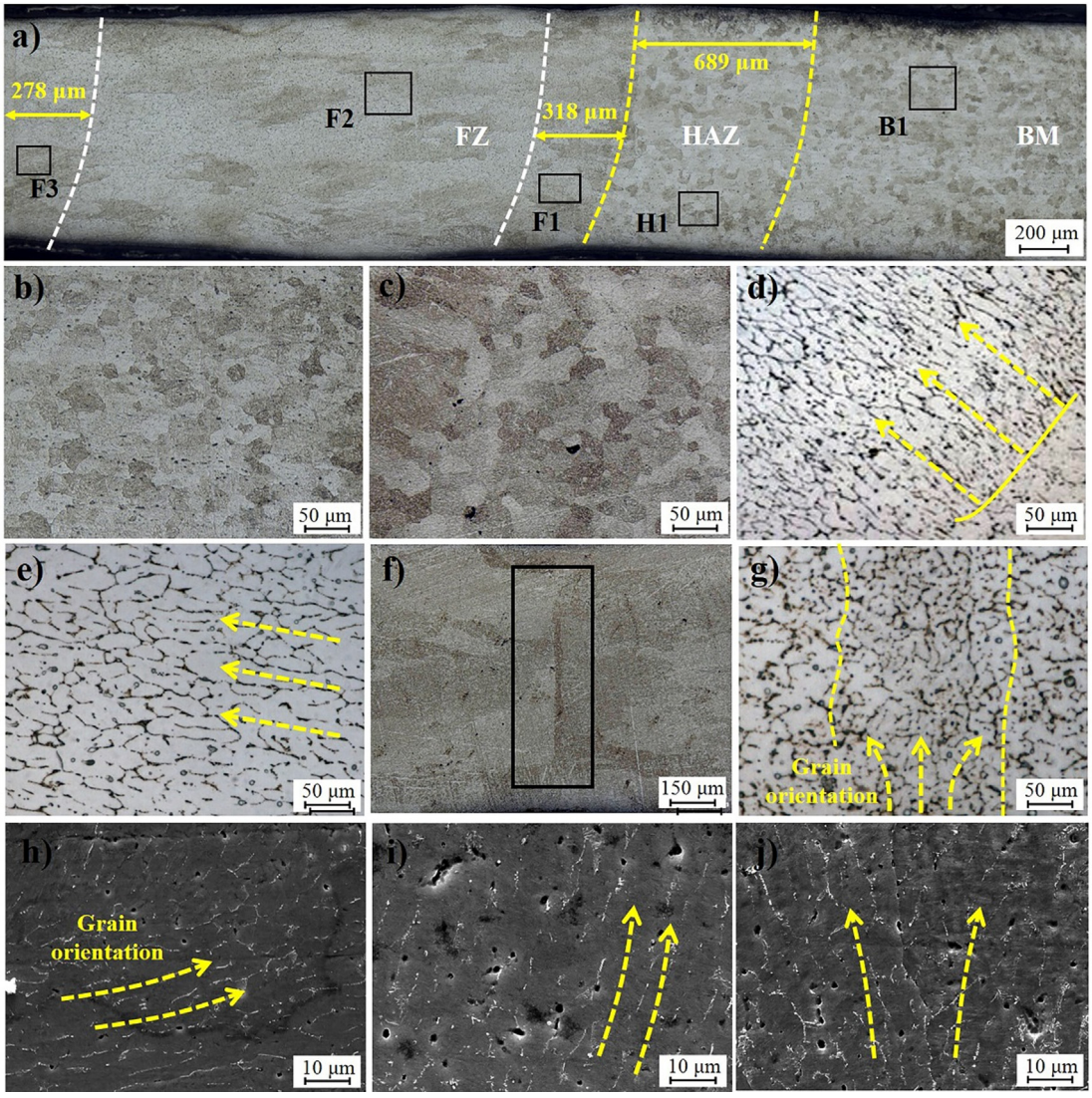

Fig. 5. The microstructure of welded joints. (a) Microstructure in different zones of welded joints. (b) Base metal zone. (c) Heat affected zone. (d) Near the fusion line zone. (e) Far from the fusion line zone. (f) The center of fusion zone. (g) The center of fusion zone (high power). (h–j). Change of grain orientation from the edge (h) to center (j) of fusion zone.

in Table 2. The segregation of titanium element occurred at the grain boundaries (position P_2) and the content fluctuation was about 5%. To further explore the titanium-rich precipitate phases (Fig. 6d and e), which showed the characteristic of rod-like shape and particle at grain boundaries, the element distribution was studied for them, which was suggested Table 2 (position P_3) and Fig. 6g-j. The precipitate phases were distributed in intermittent strips along the grain boundaries. It was found that titanium and oxygen element were enriched, which was speculated to be TiO. Meanwhile, the barren nickel in the intermittent precipitate also proved that the precipitated phase was supposed to be $NiTi_2$. Therefore, it can be concluded that the precipitates at the grain boundaries were mainly TiO and $NiTi_2$, which were all detrimental to the strength and toughness of grain boundaries in view of their brittleness.

The phase transition temperature of nitinol shape memory alloy was closely related to the content of nickel. When the content of nickel was decreased by 0.1%, the transformation temperature of M_s was increased by 12 K [6]. The precipitation of brittle phase inevitably led to the change. In addition, the transformation temperature was related to the grain size, impurity, micro stress and microdefects. The microdefects were also able to inhibit the transformation of martensite, which would be analyzed in the microdefects part. The transformation temperature of M_s within the welded joint was increased by 10 K. The abnormal change was related to the microstructure and grain size of the welded joint. Due to the increased grain size, the number of grain boundaries of phase B2 was decreased. The inhibition effect on the transformation of martensite was reduced, which promoted the transformation of martensite, leading to the increase in the temperature of M_s.

Micro defects analysis

The microstructure of the welded joints was analyzed by TEM. The analysis of electron backscatter diffraction is shown in Fig. 7. A lot of acicular martensite existed in fusion zone, which belonged to the monoclinic B19′ structure. The kernel average mismatch degree (KAM) calculated from EBSD data, which was an effective means to evaluate the local lattice distortion, was used to qualitatively describe the local strain distribution inside grains, as shown in Fig. 7c. In the figure, color blue represented the region with the minimum local lattice distortion with the Kam value ranging from

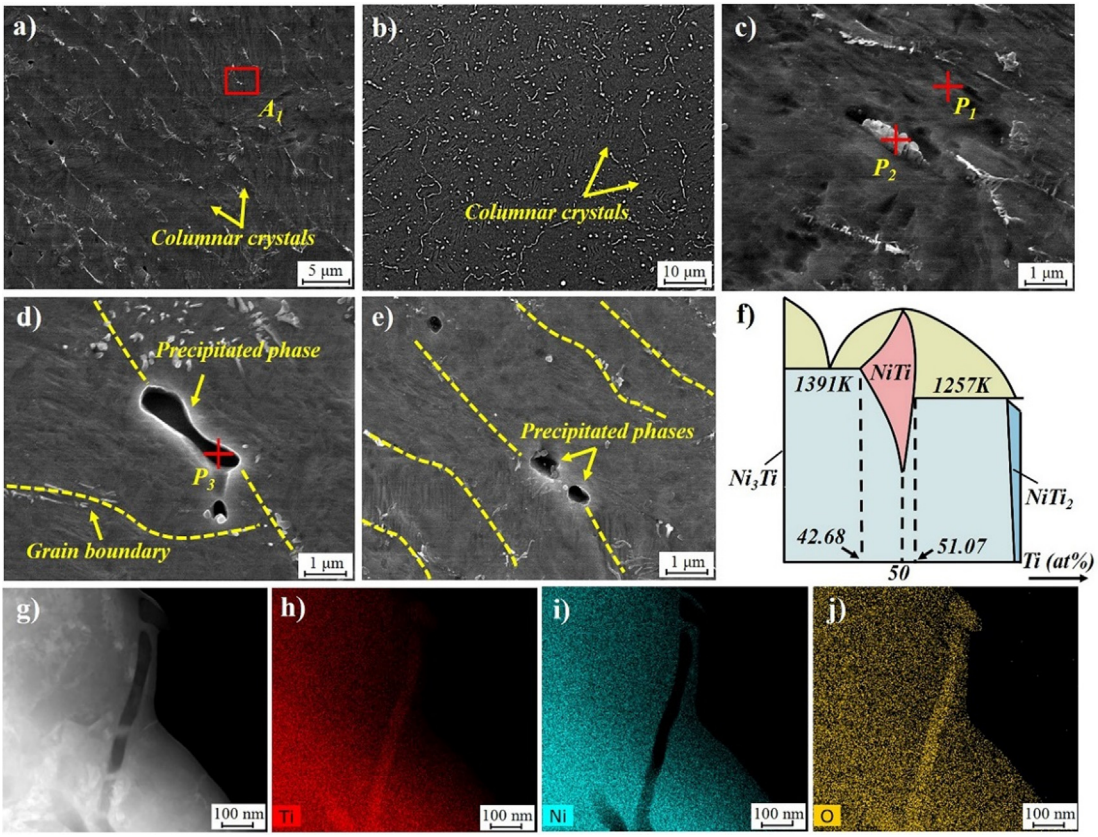

Fig. 6. Microstructure and element distribution of fusion zone. (a) Columnar crystals at the edge of fusion zone. (b) Columnar crystal in the center of fusion zone. (c) The microstructure of fusion zone. (d) The rod-like precipitate. (e) The globular precipitate. (f) Phase diagram of Ni-Ti binary alloy. (g) The precipitate phase at grain boundaries. (h) Titanium element. (i) Nickel element. (j) Oxygen element.

Table 2
Element contents (at%).

Position	Ti, (at%)	Ni, (at%)
P_1	48.85	51.55
P_2	53.61	46.39
P_3	64.07	35.93
P_4 (Base metal)	49.14	50.86

0 to 1. Color red represented the region with the largest local lattice distortion, of which the range of Kam value was 4 to 5. Other colors indicated the characteristic of moderate local lattice distortion. The closer the color was to red, the higher the Kam value was. It can be seen that in the interior of acicular martensite and the interface between the martensite and the matrix, the Kam value was high, corresponding to the large local mismatch rate and the excessive lattice distortion. There were twins, dislocations and vacancy defects in the acicular martensite. At the same time, there were also large micro stresses and high strain energy in the interior of martensite, which had adverse effects on the properties of the welded joints.

A large number of dislocations were found in the fusion zone. The formation and propagation of dislocation nuclei were driven by the stress field produced by non-equilibrium solidification of welding. With the increase in dislocation density and the movement of dislocations, when it moved to acicular martensite phase, dislocation stacking occurred at the interface under the effect of high motion resistance, resulting in stress concentration in the micro area, therefore, the large stress field and lattice distortion (Fig. 7d). As stacking further, the dislocations in the front of the interface cut into the martensite phase under the larger driving force and induced the dislocation loop structure, as shown in Fig. 7e. According to the Frank-Read dislocation increment mechanism, dislocation loops propagated in martensite under the effect of micro stress. At the same time, the dislocations in the matrix continued to penetrate, as shown in Fig. 7f. Finally, dislocations entangled with each other in the martensite, showing a grid-like distribution, as shown in Fig. 7g.

Martensite substructure analysis

Although many dislocations were produced in the region with large micro stress and deformation, some martensite still maintained a relatively pure structure, and the dislocations in the matrix did not penetrate into the martensite, as shown in Fig. 8a, b. The high-resolution picture of martensite is shown in Fig. 8c. The region A in the Fig. 7c was Fourier transformed and the diffraction pattern is shown in Fig. 7d. The substructure of the martensite was determined to be twins by diffraction spots. It was determined that the twins were characterized by mirror symmetry, of which the twins' plane was $(1\,\bar{1}\,1)$ crystal plane, and the twin angle was 31°. It was $\{11\,\bar{1}\}$ I type twins, which was lattice invariant shear, as shown in Fig. 7e. According to the analysis of the atomic arrangement of twins, stacking faults were identified in the twin martensite, which destroyed the integrity of the thermoelastic martensite structure. Due to the rapid cooling rate of electron beam welding and the metastable process of non-equilibrium

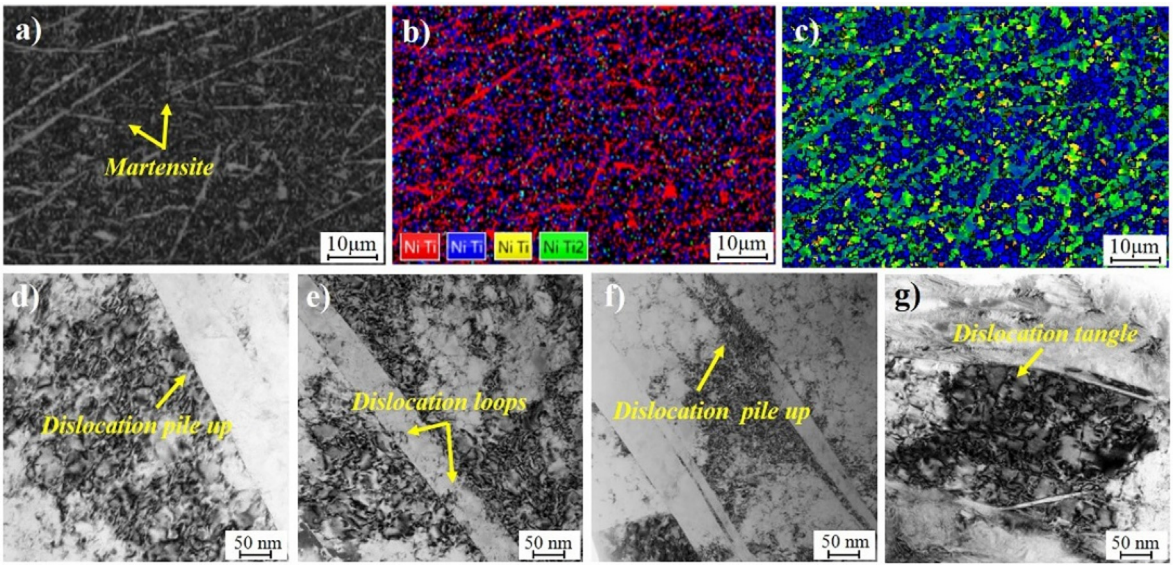

Fig. 7. Martensite phase and dislocations in fusion zone. (a) Martensite phase in fusion zone. (b) Martensite phase. (c) The diagram of kernel average mismatch. (d) Dislocation stacking in interface of martensite. (e) Dislocation loops. (f) Dislocation propagation in martensite. (g) Dislocation entanglement and network distribution.

solidification, the twins were deficiently formed. The twin interface is shown in Fig. 8f. In view of the investigation ranging three atomic layers in the twin interface, some lattice distortion was observed to be present, which lead to the micro stress field and, therefore, the deteriorated shape memory function of welded joint. In addition to the martensite with twin substructure, stacking faults existed in the martensite substructure, as shown in Fig. 8g. The high-resolution and diffraction pattern of region C are shown in Fig. 8h, indicating that the substructure was stacking faults. Considering the susceptibility of the shape memory function on the fixed orientation relationship between thermoelastic martensite and matrix, there was a disadvantageous effect on shape memory function, since the stacking faults martensite were detrimental to the thermoelastic function (Fig. 8i).

Different from the martensite observed above, a bending martensite phase was found in the fusion zone. Some martensite showed single bending characteristic and some were characterized by multiple bending, as shown in Fig. 9a, b. The twinning type of martensite was determined as shown in Fig. 9d, e. It can be seen that the substructure of bent martensite was mirror symmetry twins with symmetry angle of 5°, of which the twin plane was (100). It was the (100) composite deformation twins [32]. At the same time, there were stacking faults in the twin structure, which destroyed the integrity of twin martensite and caused local lattice distortion with micro stress field. In addition, the secondary twin structure was found in the martensite substructure, which was related to the local stress concentration [33]. Under the micro stress, the lattice orientation of primary twins was adjusted to a small angle, which was related to the effect of dislocations, stacking faults and twin boundary. The existence of secondary twins also destroyed the integrity of twin martensite structure.

The formation mechanism of bending martensite is shown in Fig. 9f, in which the circles and squares represented titanium and nickel atoms, respectively. The blue one was the atomic position projected on $(1\bar{2}0)$ plane, and the gray one was the atomic position projected on $(1\bar{2}0)$ plane. The arrangement of atoms before shear deformation is shown in the first figure. At this time, the martensite was subjected to the shear force of τ_1 on (100) plane, where the shear deformation occurred, as shown in the second figure. The martensite was bent once, as shown in Fig. 9b. When the bending times of martensite were more than one, the martensite was subjected to the shear force of τ_2 at a certain angle with (120) plane, where the second shear deformation occurred, as shown in Fig. 9a. The bending times of martensite were related to the micro stress field at this position, and the substructure of martensite twins were deformation twins.

Mechanism of shape memory performance deterioration

The deterioration mechanism of shape memory function present by electron beam welded joint of $Ni_{50}Ti_{50}$ shape memory alloy was analyzed, as shown in Fig. 10. Due to electron beam welding was a rapid process of melting and solidification, the liquid metal in the molten pool was in the metastable state of non-equilibrium solidification. A large number of defects, such as vacancies, dislocations and stacking faults, as a result, were produced. These defects were not only detected in the matrix, but also identified in the internal and interface of martensite, which damaged the integrity of thermoelastic martensite. There were a lot of dislocation defects in the matrix where the lattice distortion was large. Therefore, the dislocation stacking occurred at the martensite interface, as shown in Fig. 10a. According to the theory of dislocation stacking, if the force of moving forward cannot overcome the force of obstacle (the obstacle is referred to martensite phase interface in the study), the dislocation will stop, corresponding to the dislocation stacking. The dislocation close to the obstacle is called the leading dislocation. The more dislocations are stacked, the greater the force of leading dislocation on the obstacle. When reaching a certain degree, the leading dislocation will cut through the phase interface and enter into the martensite to form a dislocation loop structure, which will cause the dislocation source to start in the martensite. Dislocation propagation was carried out by

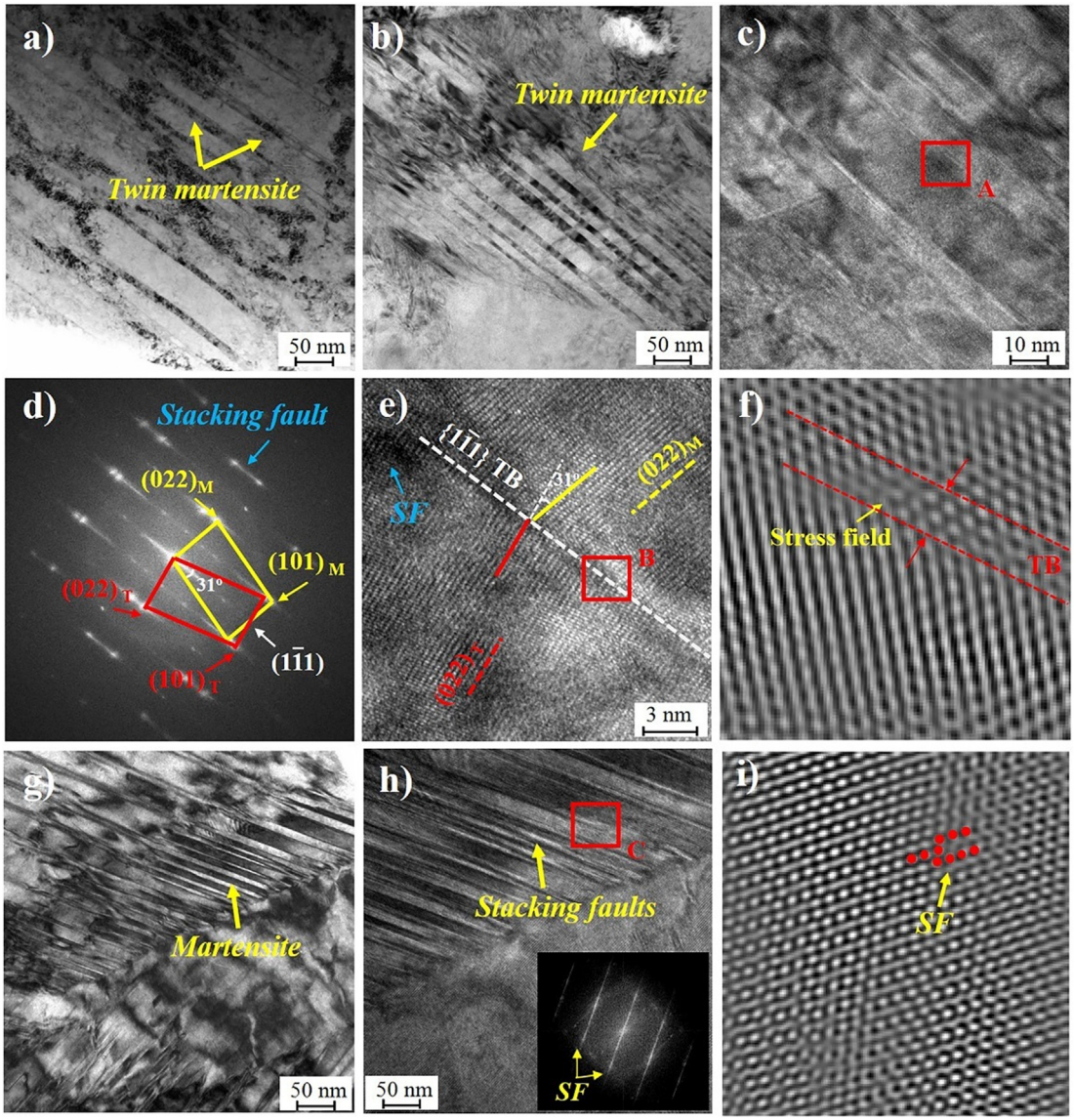

Fig. 8. Martensite phase analysis. (a, b) Martensite with twin substructure. (c) High-resolution diagram of martensite phase. (d) Diffraction pattern of martensite. (e) Twin structure of martensite. (f) Atomic arrangement of twin plane. (g) Martensite with stacking fault substructure. (h) High-resolution and diffraction pattern of stacking fault martensite. (i) Arrangement of stacking fault atoms.

Frank-Read mechanism, as shown in Fig. 10b. As further propagating, the dislocations expanded basically into the whole martensite, which destroyed the internal structure of martensite, and then affected the memory function of welded joint, as shown in Fig. 10c.

In addition, the grain size (d) of the fusion zone was smaller than that of the base metal. Since the grain size (d) of the sample remained unchanged, the d/D of the welded joint was smaller than that of the base metal, and the number of grain boundaries was unable to undergo phase transition in the fusion zone increases [34]. The decrease in grain size and the higher dislocation density in the fusion zone led to the higher Schmidt factor (m) of welded joint. As the dislocation slip resistance was increased, the critical shear stress (τ) and the plastic deformation resistance of the joint were escalated. The flow stress in the deformation process was expressed by Taylor model.

$$\sigma = \sigma_0 + M\alpha\mu b\sqrt{\rho_l} + \sigma_b \quad (1)$$

In equation (1), α was the empirical constant, μ was the shear modulus, M was the Taylor factor, b was the Burgers vector, σ_0 was the frictional resistance, σ_b was the back stress, and ρ_l was the dislocation density in the grain. According to the Kocks and Mecking model [35], the dislocation density ρ_l in grains satisfied the evolution equation of increasing plastic strain.**

$$\frac{\partial \rho_l}{\partial \varepsilon^P} = M\left(\frac{k}{d_G} + k_1\sqrt{\rho_l} - k_2\rho_l\right) \quad (2)$$

M was the Taylor factor, k=1/b, k_1=ψ/b, k_2=$k_{20}(\dot{\varepsilon}^P/\dot{\varepsilon}_0)^{-1/n}$, ψ was the scale factor, k_{20} and $\dot{\varepsilon}_0$ were constants. The first and second terms on the right side of the equation were related to heat storage, and the third term was related to dislocation annihilation in dynamic process.

It can be seen that in the process of tensile deformation, it needed more stress to reach the specified deformation, which led to the decrease in super elastic recovery rate after unloading [36]. The underlying cause was the larger shrinkage deformation,

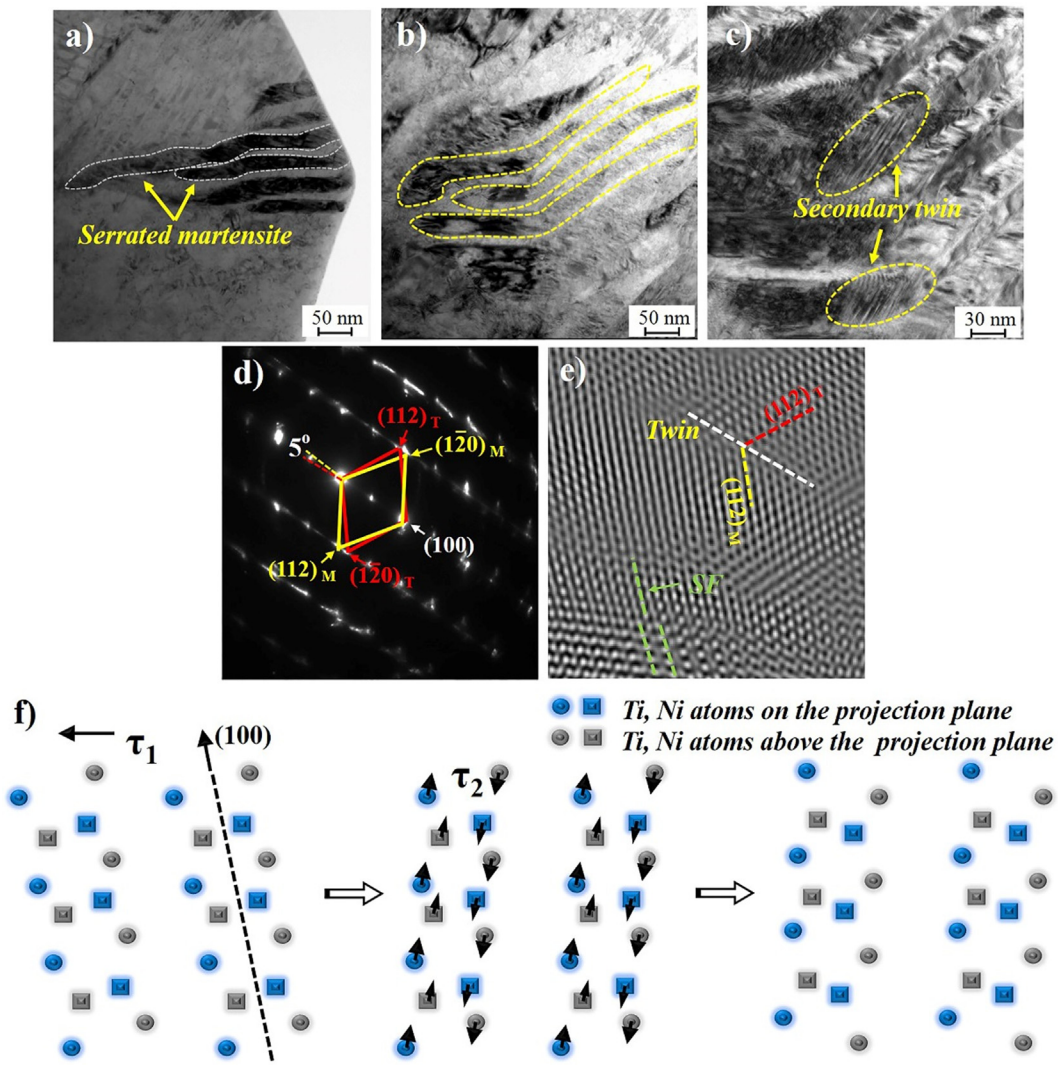

Fig. 9. Serrated martensite and formation mechanism. (a, b) Serrated martensite. (c) Secondary twins. (d) Diffraction pattern of serrated martensite. (e) Twin structure of martensite and stacking faults. (g) Formation mechanism of bending martensite.

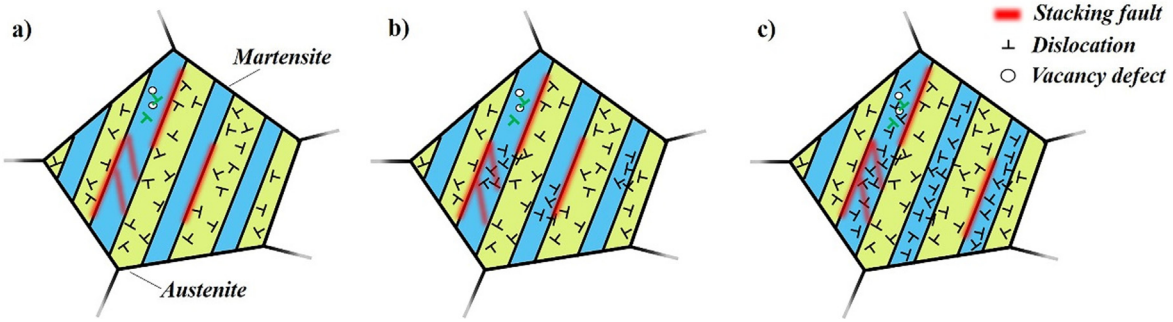

Fig. 10. Weakening Mechanism of shape memory effect. (a) Dislocation stacking stage. (b) Leading dislocation cut in. (c) Dislocation propagation stage.

which also explained the larger plastic deformation of welded joint.

Conclusions

In this paper, the mechanism of shape memory function deterioration of nitinol alloy under non-equilibrium solidification of electron beam welding was studied. The main conclusions are as follows:

1. The transformation temperature of martensite was decreased by 5 K, in contrast to the 16 K increase in transformation temperature of austenite, due to the precipitation of $NiTi_2$, the change in grain size and the increase in micro defects during different electron beam welding processes.
2. The shape memory function of welded joints was deteriorated. When the strain was 4%, the shape recovery of welded joint was only 2% of base metal. As the deformation was increased to 8%, the shape recovery of welded joint remained stable. Competing

mechanisms existed between the effect of strain and nonequilibrium solidification on the deterioration of the shape memory function.

3. The failure model of martensite twin substructure caused by leading dislocation penetration was proposed. The micro stress field produced by non-equilibrium solidification in molten pool promoted the formation and propagation of dislocations. Dislocation stacking occurred at the interface of martensite. When the interface was too overburdened to bear the stacked dislocations, the martensite was cut into by the leading dislocations, increasing the dislocation density in the martensite. Dislocations intertwined with each other in a network structure, which destroyed the integrity of martensite substructure.
4. The failure mechanism of micro defects on the integrity of martensite was revealed. The twin substructure of martensite was deficiently formed under non-equilibrium solidification, which was often accompanied by vacancies, dislocations, stacking faults, and a consequently large stress field formed between twin planes due to lattice distortion. Secondary twin was identified inside martensite under micro shear stress, where the martensite showed the bending state. These micro defects destroyed the function of the alloy.

Compliance with Ethics Requirements

This article does not contain any studies with human or animal subjects.

Declaration of Competing Interest

The authors declare that they have no known competing financial interests or personal relationships that could have appeared to influence the work reported in this paper.

Acknowledgement

The authors thank the National Natural Science Foundation of China (grant no. 51774106) for the financial support of this study.

References

[1] Burdet P, Vannod J, Hessler-Wyser A, et al. Three-dimensional chemical analysis of laser-welded NiTi–stainless steel wires using a dual-beam FIB. Acta Mater 2013;61:3090–8.
[2] Zhang W, Ao S, Oliveira JP, et al. On the metallurgical joining mechanism during ultrasonic spot welding of NiTi using a Cu interlayer. Scripta Mater 2020;178:414–7.
[3] Kato H, Yasuda Y, Sasaki K, et al. Thermodynamic assessment of the stabilization effect in deformed shape memory alloy martensite. Acta Mater 2011;59:3955–64.
[4] Padhy GK, Wu CS, Gao S. Friction stir based welding and processing technologies – processes, parameters, microstructures and applications: a review. J Mater Sci Technol 2018;34(1):1–38.
[5] Oliveira JP, Zeng Z, Andrei C, et al. Dissimilar laser welding of superelastic NiTi and CuAlMn shape memory alloys. Mater Design 2017;128:166–75.
[6] Falvo A, Furgiuele FM, Maletta C. Laser welding of a NiTi alloy: mechanical and shape memory behavior. Mat Sci Eng A-Struct 2005;412(1):235–40.
[7] Oliveira JP, Fernandes FMB, Miranda RM, et al. Residual stress analysis in laser welded NiTi sheets using synchrotron X-ray diffraction. Mater Design 2016;100:180–7.
[8] Bahador A, Hamzah E, Kondoh K, et al. Mechanical and superelastic properties of laser welded Ti–Ni shape-memory alloys produced by powder metallurgy. J Mater Process Tech 2017;248:198–206.
[9] Falvo A, Furgiuele FM, Maletta C. Functional behaviour of a NiTi-welded joint: Two-way shape memory effect. Mat Sci Eng A-Struct 2008;481:647–50.
[10] Mani P, Perugu C, Hc M, et al. Exploring the functional and corrosion behavior of friction stir welded NiTi shape memory alloy. J Manuf Process 2019;47:119–28.
[11] Wagner MX, Dey S, Gugel H, et al. Effect of low-temperature precipitation on the transformation characteristics of Ni-rich NiTi shape memory alloys during thermal cycling. Intermetallics 2010;18(6):1172–9.
[12] Wang X, Kustov S, Verlinden B, et al. Fundamental development on utilizing the R-phase transformation in NiTi shape memory alloys. Shape Mem Superelasticity 2015;1(2):231–9.
[13] Bojda O, Eggeler G, Dlouhý A. Precipitation of Ni4Ti3-variants in a polycrystalline Ni-rich NiTi shape memory alloy. Scr Mater 2005;53(1):99–104.
[14] Oliveira JP, Miranda RM, Fernandes FMB. Welding and joining of NiTi shape memory alloys: a review. Prog Mater Sci 2017;88(7):412–66.
[15] Shamsolhodaei A, Zhou YN, Michael A. Enhancement of mechanical and functional properties of welded NiTi by controlling nickel vaporization. Sci Technol Weld Joi 2019;24(8):1–7.
[16] Oliveira JP, Fernandes FMB, Miranda RM, et al. Effect of laser welding parameters on the austenite and martensite phase fractions of NiTi. Mater Charact 2016;119:148–51.
[17] Fei X, Grummon DS, Ye C, et al. Surface form memory in NiTi shape memory alloys by laser shock indentation. J Mater Sci 2012;47(5):2088–94.
[18] Mehrpouya M, Gisario A, Elahinia M. Laser welding of NiTi shape memory alloy: A review. J Manuf Process 2018;31:162–86.
[19] Kannan D, Sathiya P, Ramesh T. Experimental investigation and characterization of laser welded Nitinol shape memory alloys. J Manuf Process 2017;25(1):253–61.
[20] Song YG, Li WS, Li L, et al. The influence of laser welding parameters on the microstructure and mechanical property of the as-jointed NiTi alloy wires. Mater Lett 2008;62(15):2325–8.
[21] Tam B, Khan MI, Zhou Y. Mechanical and functional properties of laser-welded Ti-55.8 Wt Pct Ni nitinol wires. Metall Mater Trans A 2011;42(8):2166–75.
[22] Niu H, Jiang HC, Zhao MJ, et al. Effect of interlayer addition on microstructure and mechanical properties of NiTi/stainless steel joint by electron beam welding. J Mater Sci Technol 2021;61:16–24.
[23] Yang D, Jiang HC, Zhao MJ, et al. Microstructure and mechanical behaviors of electron beam welded NiTi shape memory alloys. Mater Design 2014;57:21–5.
[24] Chan CW, Man HC, Cheng FT. Fatigue behavior of laser-welded NiTi wires in small-strain cyclic bending. Mat Sci Eng A-Struct 2013;559(1):407–15.
[25] Zamani N, Khamesee MB, Khan MI. Novel laser processed shape memory alloy actuator design with an embedded strain gauge sensor using dual resistance measurements. Part I: Fabrication and Model-Based Position Estimation. Sensor Actuat A-Phys 2020;313(1):112188.
[26] Bram M, Ahmad KA, Heckmann A, et al. Powder metallurgical fabrication processes for NiTi shape memory alloy parts. Mat Sci Eng A-Struct 2002;337:254–63.
[27] Dolce M, Cardone D. Mechanical behaviour of shape memory alloys for seismic applications 2. Austenite NiTi wires subjected to tension. Int J Mech Sci 2001;43:2657–77.
[28] Mirshekari GR, Saatchi A, Kermanpur A, et al. Laser welding of NiTi shape memory alloy: Comparison of the similar and dissimilar joints to AISI 304 stainless steel. Opt Laser Technol 2013;54:151–8.
[29] Khan MI, Zhou Y. Effects of local phase conversion on the tensile loading of pulsed Nd: YAG laser processed Nitinol. Mat Sci Eng A-Struct 2010;527:6235–8.
[30] Tuissi A, Besseghini S, Ranucci T, et al. Effect of Nd-YAG laser welding on the functional properties of the Ni-49.6 at.% Ti. Mat Sci Eng A-Struct 1999;273–275:813–7.
[31] Sevilla P, Martorell F, Libenson C, et al. Laser welding of NiTi orthodontic arch wires for selective force application. J Mater Sci Mater Med 2008;19(2):525–9.
[32] Onda T, Bando Y, Ohba T, et al. Electron Microscopy Study of Twins in Martensite in a Ti-50.0 at%Ni Alloy. Mater Trans 1992;33(4):354–9.
[33] Hu L, Jiang S, Liu S, et al. Transformation twinning and deformation twinning of NiTi shape memory alloy. Mat Sci Eng A-Struct 2016;660(13):1–10.
[34] Xu B, Kang GZ, Yu C, et al. Phase field simulation on the grain size dependent super-elasticity and shape memory effect of nanocrystalline NiTi shape memory alloys. Int J Eng Sci 2020;156:103373.
[35] Kocks UF, Mecking H. Physics and phenomenology of strain hardening: the FCC case. Prog Mater Sci 2003;48(3):171–273.
[36] Ahadi A, Sun Q. Effects of grain size on the rate-dependent thermomechanical responses of nanostructured superelastic NiTi. Acta Mater 2014;76:186–97.